The Revisited Frequency-Shift Method for Shear Wave Attenuation Computation and Imaging

Ladan Yazdani, Manish Bhatt, Iman Rafati, An Tang, and Guy Cloutier, *Senior Member, IEEE*

***Abstract*— Ultrasound (US) shear wave (SW) elastography has been widely studied and implemented on clinical systems to assess the elasticity of living organs. Imaging of SW attenuation reflecting viscous properties of tissues has received less attention. A revisited frequency shift (R-FS) method is proposed to improve the robustness of SW attenuation imaging. Performances are compared with the FS method that we originally proposed and with the two-point frequency shift (2P-FS) and attenuation measuring US SW elastography (AMUSE) methods. In the proposed R-FS method, the shape parameter of the gamma distribution fitting SW spectra is assumed to vary with distance, in contrast to FS. Second, an adaptive random sample consensus (A-RANSAC) line fitting method is used to prevent outlier attenuation values in the presence of noise. Validation was made on ten simulated phantoms with two viscosities (0.5 and 2 Pa·s) and different noise levels (15 to −5 dB), two experimental homogeneous gel phantoms, and six *in vivo* liver acquisitions on awake ducks (including three normal and three fatty duck livers). According to the conducted experiments, R-FS revealed mean reductions in coefficients of variation (CV) of 62.6% on simulations, 62.5% with phantoms, and 62.3% *in vivo* compared with FS. Corresponding reductions compared with 2P-FS were 45.4%, 77.1%, and 62.0%, respectively. Reductions in normalized root-mean-square errors for simulations were 63.9% and 48.7% with respect to FS and 2P-FS, respectively.**

***Index Terms*— Attenuation measuring ultrasound (US) shear wave (SW) elastography (AMUSE), fatty liver, frequency shift (FS), SW attenuation, SW elastography, two-point frequency shift (2P-FS), ultrasonography.**

I. INTRODUCTION

ULTRASOUND (US) shear wave (SW) elastography is an established technology that utilizes a clinical US system to noninvasively assess the mechanical properties of soft tissues [1]. This technique is based on the monitoring of SW propagation in biological tissues. SWs can be generated within the target tissue by focusing US push beams using a remote US probe [2]–[4]. The US probe first generates an acoustic radiation force that induces transient SWs in the tissue, and then, detecting the SW motion is done via tracking algorithms [5]. Faster propagation of SWs in stiffer tissues than softer ones has been used to characterize the severity of diffuse liver disease and focal lesions [6]–[8]. In recent years, SW attenuation is receiving attention to characterize biological tissues [9]–[11]. SW speed and attenuation are the basic properties of viscoelastic tissues that can be used for pathological organ diagnosis [7], [8].

The stiffness of a purely elastic medium is often quantified in terms of its Young's modulus (E) given as $E = 3\rho c^2$ (here, ρ is the medium density assumed constant and c is the SW speed). However, biological tissues are inherently viscoelastic in nature as they behave both as solid-like and fluid-like materials [12]. Past studies have utilized the SW speed frequency dispersion to estimate viscoelasticity through the assumption of a rheological model [often Kelvin–Voigt (KV)] [13]–[16]. Kazemirad *et al.* [17] proposed a rheological model-free method for quantifying the frequency-dependent shear modulus, under the assumption of a homogeneous and isotropic medium, and a cylindrical SW propagation front to correct for wave diffraction. A similar diffraction correction method was proposed by Budelli *et al.* [18] using similar hypotheses. There are also some other estimators of tissue viscoelastic properties, such as group SW speed (gSWS) [19], fractional derivative gSWS [20], and reverberant SW [21].

Manuscript received March 16, 2022; accepted April 7, 2022. Date of publication April 11, 2022; date of current version May 26, 2022. This work was supported in part by the Fonds de Recherche Québec (Audace Program) under Grant #2019-AUDC-263591, in part by the Onco-Tech Program, in part by the Fonds de Recherche Québec Santé (FRQS), in part by Oncopole, in part by Medteq, in part by TransMedTech, in part by Cancer Research Society, and in part by Siemens Healthcare. The work of An Tang was supported by FRQS and Fondation de l'Association des Radiologistes du Québec under Grant #298509. *(Corresponding author: Guy Cloutier.)*

This work involved animals in its research. Approval of all ethical and experimental procedures and protocols was granted by the Institutional Animal Care Committee of the University of Montreal Hospital Research Center under Assurance No. A5377-01, and performed in line with the guidelines on the care and use of laboratory animals issued by the Canadian Council on Animal Care and the U.S. National Institutes of Health.

Ladan Yazdani and Iman Rafati are with the Laboratory of Biorheology and Medical Ultrasonics (LBUM), University of Montreal Hospital Research Centre (CRCHUM), Montreal, QC H2X 0A9, Canada, and also with the Institute of Biomedical Engineering, University of Montreal, Montreal, QC H3T 1J4, Canada (e-mail: ladan.yazdani@umontreal.ca; iman.rafati@umontreal.ca).

Manish Bhatt was with the Laboratory of Biorheology and Medical Ultrasonics (LBUM), CRCHUM, Montreal, QC H2X 0A9, Canada. He is now with the Department of Electronics and Electrical Engineering, IIT Guwahati, Guwahati 781039, India (e-mail: manish49bhatt@gmail.com).

An Tang is with the Laboratory of Clinical Image Processing, CRCHUM, Montreal, QC H2X 0A9, Canada, also with the Department of Radiology, University of Montreal Hospital, Montreal, QC H2X 0C1, Canada, and also with the Department of Radiology, Radiation Oncology, and Nuclear Medicine, University of Montreal, Montreal, QC H3T 1J4, Canada (e-mail: an.tang@umontreal.ca).

Guy Cloutier is with LBUM, CRCHUM, Montreal, QC H2X 0A9, Canada, and also with the Department of Radiology, Radiation Oncology, and Nuclear Medicine, and the Institute of Biomedical Engineering, University of Montreal, Montreal, QC H3T 1J4, Canada (e-mail: guy.cloutier@umontreal.ca).

This article has supplementary downloadable material available at https://doi.org/10.1109/TUFFC.2022.3166448, provided by the authors.

Digital Object Identifier 10.1109/TUFFC.2022.3166448

State-of-the-art alternative methods for viscoelasticity estimation rely on SW attenuation computation [9]–[11], [22], which has been a challenge due to variance under noisy conditions [23]. The attenuation measuring US shear-wave elastography (AMUSE) method improved robustness to noise by using a 2-D k-space frequency analysis within a region-of-interest (ROI) [10]. However, this approach does not provide imaging capability due to the requirement of analyzing the whole ROI to provide an estimate. As other SW attenuation methods [9], [23], it does not assume any rheological model, and the hypothesis of a linear, homogeneous, and isotropic viscoelastic medium remains a requirement for AMUSE.

The frequency-shift (FS) method proposed by Bernard *et al.* [9] to image SW attenuation was built on the hypothesis that geometrical diffraction spreading effects are independent of the SW frequency and that attenuation depends linearly on frequency. Consequently, the FS method does not require the acoustic radiation force source to be planar (i.e., infinitely long) or cylindrical. The main novelty of this work was to hypothesize that the frequency domain amplitude spectrum of SWs follows a gamma distribution, and that the rate parameter of this gamma fit is related to SW attenuation by a linear relation. However, in its current form, retrieving the rate parameter by a linear frequency fitting can be challenging under noisy conditions. Kijanka and Urban [23] proposed a modification to the FS method (named two-point frequency shift method—2P-FS), in which data from only two spatial locations are utilized to estimate attenuation. However, limitations exist in terms of optimum selection of these two points, which is a concern for achieving accuracy in SW attenuation computation.

In this study, we implemented the state-of-the-art SW attenuation methods (FS, 2P-FS, and AMUSE) and revisited our original implementation of FS (named R-FS) by making the following contributions [24]: first, the assumption of a constant shape parameter for all lateral locations was dropped, as also proposed in [23] and second, an adaptive random sample consensus (A-RANSAC) algorithm [25] was developed to estimate the slope of the varying rate parameter with distance of the gamma distribution. The advantage of these modifications is that instead of selecting only two spatial points in an ROI as for the 2P-FS method, the proposed approach can consider multiple spatial locations to award more accuracy.

II. METHODS

A. FS Algorithm

The FS method [9] is briefly reviewed here. Assuming that the SW field amplitude spectrum at location x_0 is $S(f)$, then after a distance Δx away from this location, i.e., at $x_1 = x_0 + \Delta x$, the amplitude spectrum can be written as

$$|R(f)| = G(f, x_1) \times H(f, \Delta x) \times |S(f)| \tag{1}$$

where $G(f, x_1)$ represents the geometrical diffraction effects, and $H(f, \Delta x)$ is the viscous attenuation of the SW amplitude. The geometrical spreading can be nullified by assuming that $G(f, x_1)$ is independent of the SW frequency. By considering a linear relation with frequency of the SW attenuation, $H(f, \Delta x)$ becomes

$$H(f, \Delta x) = \exp(-\alpha_0 \times f \times \Delta x) \tag{2}$$

where α_0 is the linear attenuation coefficient. In (1), the SW amplitude spectrum is described by a gamma distribution, as validated in [26]. It can be expressed as

$$|S(f)| \propto A f^{k_0-1} e^{-f\beta_0} \tag{3}$$

where A is the amplitude parameter of the gamma distribution, k_0 is the shape parameter that controls the symmetry of the distribution, and β_0 is the rate parameter. From (1)–(3), the SW amplitude spectrum at location x_1 becomes

$$|R(f)| \propto A f^{k_0-1} e^{-f(\beta_0+\alpha_0\Delta x)}. \tag{4}$$

Here, the linear relation $\beta(\Delta x) = \beta_0 + \alpha_0 \Delta x$ corresponds to the rate parameter computed on a distance Δx. The parameter α_0 is the slope of the varying rate parameter. As described next, a three-parameter nonlinear least-square (LSQ) optimization was performed at each lateral location in the x-direction to estimate the amplitude, shape, and rate parameters of the gamma distribution in (4)

$$[A, k_0, \beta(\Delta x)] = \arg\min_{A,k_0,\beta} \|R(f, x_1) - R(f, x_0)\|_2^2. \tag{5}$$

After estimating $\beta(\Delta x) = \beta_0 + \alpha_0 \Delta x$ for each location between x_0 and $x_0 + \Delta x$, a linear fit was performed between the rate parameter and spatial locations. The slope of this line is the SW attenuation coefficient (α_0).

B. 2P-FS Algorithm

This method [23] corresponds to an improved version of FS [9], for which only two spatial locations were utilized to compute SW attenuation instead of multiple lateral points over a selected lateral length. Kijanka and Urban [23] also proposed using varying shape parameters of the gamma distribution for each pair of the first and second signal positions to consider the difficulty of keeping that parameter equal for both source and attenuated amplitude spectra in all lateral positions. The main advantage of considering only two points is that it reduces the computational burden. Another advantage is that it may help avoiding noisy outliers that may exist between these two points. Computations can be performed for various first signal positions and distances between two lateral positions.

However, one weakness of the 2P-FS method is the ambiguity on how to select the two points along distance. Selection of two optimum positions can be extremely challenging in anisotropic and heterogeneous biological tissues (even if the assumption of a homogeneous isotropic tissue is considered for FS methods). If the two points are not selected properly, estimated parameters of the gamma distribution [see (5)] might be biased. Another concern is that selecting only two points in a lateral direction may correspond to a small sample size for performing a linear fitting and may consequently result in a lower accuracy. In the proposed study, the selection of the two points was done based on the map obtained by selecting various pairs of points laterally and by averaging them at the focal depth.

C. R-FS Algorithm

In this study, we propose two modifications to the original FS method [9]. These improvements deal with the inverse problem of (5) and aim at improving the estimation of the rate (β_0) and slope (α_0) parameters with respect to lateral distance. First, a nonlinear LSQ algorithm (Levenberg–Marquardt) was used to solve (5). In [9], the shape parameter (k_0) was assumed to be constant for each lateral location. However, we have dropped this assumption, as also suggested in [23]. Once amplitude, shape, and rate parameters were computed for each lateral location using (5), linear fits were performed to estimate slopes (α) with respect to lateral distances (i.e., β versus x). Unlike the 2P-FS method where only two lateral locations were considered, the proposed modification performed computations at multiple points along the lateral direction.

Second, an A-RANSAC algorithm was used to avoid noisy/false outliers in the estimation of the linear slope of rate parameters (β) versus lateral distance. The RANSAC algorithm is an iterative line fitting method with improved robustness to large numbers of outliers [25]. It has been previously utilized in processing US images [27]–[29]. For more details about the classical RANSAC implementation, readers are referred to [25].

The algorithm for the proposed method is summarized in Fig. 1. We made two modifications in the implementation of RANSAC for linear fitting of rate parameters with distances of the gamma distribution model. The original RANSAC algorithm selects two points randomly and uses a preset threshold. Here, instead of selecting the two points randomly, all combinations of two points are chosen, which is convenient due to the limited number of computed rate parameters (less than 20 points based on the selected size of the ROI). Second, instead of assuming a fixed preset threshold, the threshold was automatically set based on the algorithm provided in Fig. 1.

According to this algorithm, all possible pairs of points among inliers were considered. An initial threshold ($\mathrm{Th}_{\mathrm{new}}$) was obtained in the case that half of other points (excluding the pair of points selected) were within the threshold. Therefore, with this procedure, more than half of all points were considered as inliers ($N/2 + 1$, N: number of points). This threshold was updated at each iteration aimed at selecting two new points, until the minimum threshold included more than half of points. Then, the line corresponding to this threshold corresponded to the searched line fitting of the A-RANSAC algorithm.

D. AMUSE Algorithm

For comparative purpose, the AMUSE method was implemented according to [10]. As mentioned earlier, it uses a k-space-based approach to assess the frequency dispersion of SWs. In summary, a 2-D Fourier transform of the SW displacement field $[u(x, t)]$ is computed, where x is the distance and t is the time. It is written in the k-space domain as $U(k, f)$, where k is the wavenumber and f is the frequency. For a propagating wave with a frequency f_0, the magnitude of $U(k, f)$ has a peak at $(f_0/c, f_0)$ [10]. For computing the SW attenuation, the full-width-at-half-maximum (FWHM) is computed, and the SW attenuation (α) evaluated over a range of frequency (based on the k-space magnitude maxima) becomes [10]

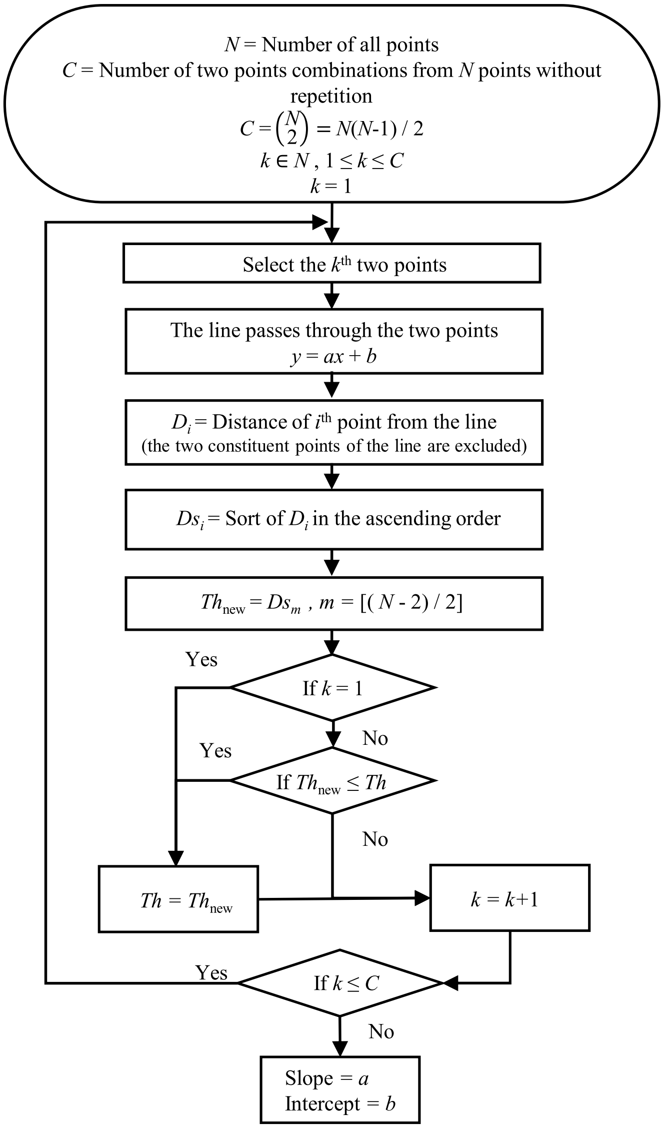

Fig. 1. A-RANSAC flowchart.

$$\alpha = \frac{\mathrm{FWHM} \times \pi}{\sqrt{3}}. \tag{6}$$

Thus, AMUSE offers a state-of-the-art analytical model to compute SW attenuation without much computational complexity. It provides a viscoelasticity measure but no images associated with it. This method is computationally very fast and efficient, and it was adopted as a reference method for comparative purpose [23]. However, only a mean value of the SW attenuation in an ROI can be computed using this approach.

E. Simulation Model

The SW propagation in two tissue mimicking materials was simulated based on the KV rheological model using

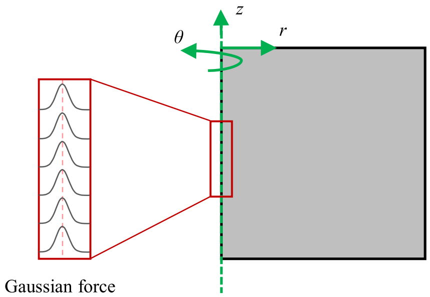

Fig. 2. Schematic of the finite-element model in COMSOL. The model is cylindrical and axisymmetric along the *z*-axis (green dashed line).

COMSOL software (version 3.5a, structural mechanics module, Palo Alto, CA, USA), as in [30]. For both media, the density was assigned to 1055 kg/m^3, the shear modulus (G) to 3.24 kPa, and Poisson's ratio to 0.499. In the first simulation, the viscosity was set to 0.5 Pa·s, and in the second, it was fixed to 2 Pa·s. The total mesh size contained 16 463 domain elements and 795 boundary elements. The SW was generated by a Gaussian force, as depicted in Fig. 2, according to [31]. To mimic experimentally collected data, Gaussian random noise (MATLAB function awgn) was added to the SW velocity field at signal-to-noise ratios (SNRs) of 15 to −5 dB. Therefore, ten noisy simulations were obtained for assessing attenuation measurement methods. Interested readers may consult Supplementary materials (Section I) for numerical SW particle velocity motion with added noise. Even though SNR values were imposed in simulated datasets, an SNR approximation method described in Appendix B was used to validate simulated and experimental conditions reported in this work.

Because the KV model was utilized in the finite elements modeling (FEM) simulations, it was, thus, considered as the gold standard for comparison of simulations. Calculations were done based on [30], and for each frequency, an attenuation was evaluated and the slope of that attenuation was considered as the attenuation coefficient of the KV model, as it was also performed in [23].

F. Attenuation Map Reconstruction

SW attenuation maps were reconstructed for the three methods described in Sections II-A–II-C: R-FS, 2P-FS, and FS. A constant rectangular ROI was considered for all three methods [Fig. 3(a)]. This ROI was selected 4 mm away from push locations, as in [9] and [26]. Within this rectangular ROI, a computing window is moving in axial and lateral directions with a predefined overlap to construct the attenuation map. The length and width of the computing windows were 4.06 mm (13 pulse lengths) and 3.98 mm (56 depth lines), respectively. The overlaps of computing windows in both axial and lateral directions were 92%. All these parameters were set the same for all methods providing maps. In each computing window, the velocity fields were averaged in the axial direction to obtain the attenuation using R-FS, 2P-FS, and FS methods. Finally, a cubic interpolation was used to increase the spatial sampling of the reconstructed map. For FS and R-FS, the attenuation was obtained based on all data points along the lateral distance in each computing window. However, 2P-FS uses only two points laterally; the distance between these two signal positions was equal to the lateral segment length of FS and R-FS. In addition, another kind of maps was constructed on a linear ROI for simulations. The ROI was selected on the averaged velocity field along the lateral distance at the focal depth [Fig. 3(b)]. In this map, the computing windows had different lengths, which could be in different positions. These maps were obtained based on the combination of different lateral positions with various lengths of the computing window [Fig. 3(b)]; they were made to be able to compare our results with [23].

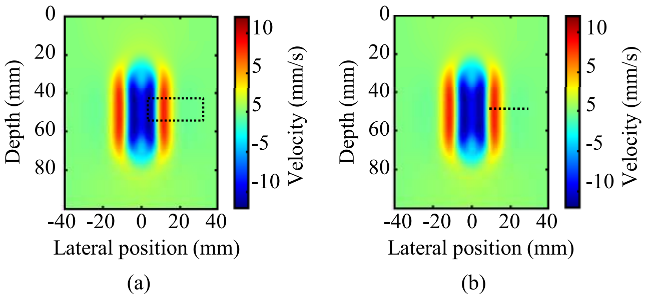

Fig. 3. Two types of ROIs used to construct maps in this study: (a) rectangular ROI is used to compute the SW attenuation over depth and lateral directions and (b) second type of map is obtained by selecting various segment lengths laterally at the focal depth.

III. MATERIALS

A. In Vitro Phantoms

Two homogeneous tissue mimicking viscoelastic phantoms were prepared using gelatin (type A, #G2500, Carolina Biological Supply, Burlington, NC, USA), dietary xanthan gum, and cellulose particles with a nominal diameter of 50 μm (Sigmacell type 50, #S5504, Sigma-Aldrich Chemical, St. Louis, MO, USA). The stiffness was driven by the gelatin concentration, xanthan gum was responsible for viscous loss properties, and cellulose particles produced acoustic scattering. The procedure to prepare tissue-mimicking phantoms is briefly summarized [26]; all proportions are in weight by weight (w/w). For the first phantom, 5% gelatin and 0.1% xanthan gum were first mixed thoroughly in a dry powder form and then added into distilled water at room temperature. For the second phantom, the xanthan gum proportion was 0.5%. Next, this solution was heated up to 90 °C while continuously stirring so that gelatin and xanthan gum were dissolved completely. The solution was naturally cooled down to 40 °C, and at this temperature, 1.5% of cellulose powder was added to act as scatterers. The solution was then allowed returning to room temperature and then cast into a rectangular box kept in an ice-water bath for fast and uniform gelation. Phantoms were kept in a refrigerator overnight for 16 h at a temperature of 4 °C to continue the gelation. The next day, samples were subsequently allowed to naturally return to room temperature (20 °C) prior to measurements.

Readers are referred to Appendix B for SNR conditions of *in vitro* phantom experiments. Values reported in Appendix B allowed comparing simulation, *in vitro* and *in vivo* conditions.

B. In Vivo Duck Liver Data

Six *in vivo* duck liver acquisitions were used for comparing the performance of FS, 2P-FS, R-FS, and AMUSE methods. The protocol was approved by the animal ethical care committee of the University of Montreal Hospital Research Centre, Montreal, QC, Canada. Three different ducks had undergone a force-feeding (FF) process to induce fatty liver [32]. Acquisitions were performed as part of the study conducted by Bhatt *et al.* [33] (12 days of FF). Radio frequency (RF) data after radiation pressure pushes were acquired before and after the FF process for each animal to provide both normal and fatty duck liver datasets. See Appendix B for SNRs of *in vivo* data.

C. US Measurements

1) Data Acquisition Procedure: Acoustic radiation force beam sequences were implemented on research US systems (models V1 and Vantage, Verasonics Inc., Redmond, WA, USA). A linear array probe (ATL L7-4, Philips, Bothell, WA) was used at a central frequency of 5 MHz to remotely generate SWs inside samples. For phantom acquisitions (V1 scanner), each sequence generated three focused pushes spaced 5 mm apart inside the sample; the first push was at a depth of 1.5 cm. The three acoustic pushes lasted 185 μs each. For *in vivo* duck liver acquisitions (Vantage scanner), five focused pushes spaced 2.5 mm apart were used, with the first push at 1 cm depth. Each push lasted 198 μs. Immediately after generating the radiation pressure, the same US transducer was used to record plane-wave compounded RF data for postprocessing (100 frames at a frame rate of 4000 Hz for phantoms and 3623 Hz for ducks).

2) Postprocessing: For all measurements, RF data were beamformed using an $f-k$ migration algorithm [34]. The particle velocity field was estimated from recorded RF data using a 2-D auto-correlation algorithm [35]. Apodization was done on time domain signals via a Tukey window [26], and a low pass filter (cutoff frequency of 650 Hz) was utilized to reduce noise outliers. A directional filter was applied to the computed velocity field to suppress SW reflections from sample boundaries/interfaces [36].

IV. RESULTS

A. Simulations

Fig. 4(a) and (b) presents estimated shape and rate parameters at varying lateral positions for simulations at an SNR of -5 dB and viscosities of 0.5 and 2 Pa·s, respectively. Fig. 4(c) and (d) presents two examples of gamma distributions fitted on these simulated datasets, for two lateral distances A and B. The goodness of the gamma fits is perused by the R-squared (R^2) value. At both viscosities for positions A and B, R^2 varied between 0.92 and 0.99.

From estimated gamma fits, the attenuation coefficient could be retrieved as the slope of rate parameters versus lateral positions. To show the performance of the proposed A-RANSAC method for linear fitting (as discussed in Section II-C), comparisons were made with the iterative reweighted LSQ regression (robustfit, MATLAB) and linear least squares (LLSQ) regression, for an SNR of -5 dB. As displayed in Fig. 5, the A-RANSAC method provided superior line fittings at both viscosities.

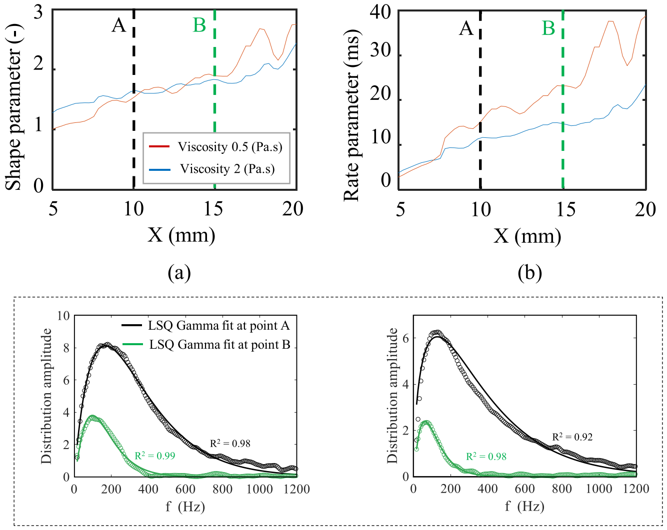

(a) (b)

(c) (d)

Fig. 4. (a) Shape (no unit) and (b) rate (ms) parameters of the gamma distribution averaged at the focal depth and estimated using LSQ regressions in the case of noisy simulations (SNR $=-5$ dB) with viscosities of 0.5 and 2 Pa·s. In (c) and (d), the circles and the continuous line present simulation data spectrum and gamma fit spectrum, respectively.

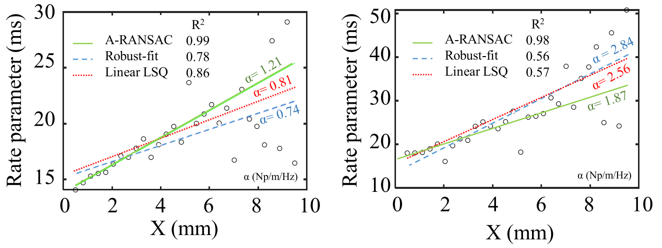

(a) (b)

Fig. 5. Comparison of regression performance of A-RANSAC versus robust-fit (iterative reweighted LSQ regression) and LLSQ regression, for simulations with viscosities of (a) 0.5 and (b) 2 Pa·s, and added Gaussian noise at an SNR of -5 dB.

To investigate the performance of R-FS, 2P-FS, and FS methods for attenuation estimation, Gaussian noise with SNRs from 15 to -5 dB was studied with numerical simulations. Reconstructed attenuation maps computed within the ROI of Fig. 3(a) are presented in Figs. 6 and 7 for both viscous conditions, respectively. Boxplots of attenuation maps are compared with AMUSE in Figs. 8 and 9 for both viscosities at different SNRs. Tabulated values of mean, standard deviation (SD), coefficient of variation (CV), and normalized root mean square error (NRMSE) with respect to ground truth (KV model) are given in Table I for FS, 2P-FS, R-FS, and AMUSE methods. R-FS remained robust with the addition of noise compared with FS and 2P-FS. Negative biases are also noticed for FS. Expected homogeneous attenuation maps are preserved when adding noise for R-FS at both viscosities, whereas good performance is seen for 2P-FS at SNR >-5 dB. Quantitatively, AMUSE performed well and gave attenuation

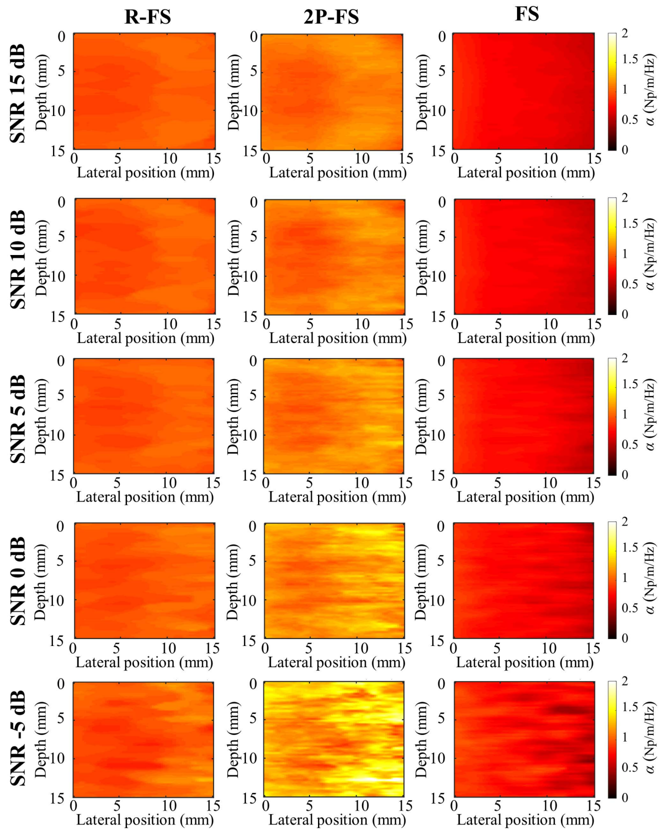

Fig. 6. Attenuation maps reconstructed for numerically simulated data with added noise (SNR of 15 to −5 dB) at a viscosity of 0.5 Pa·s for R-FS, 2P-FS, and FS imaging methods.

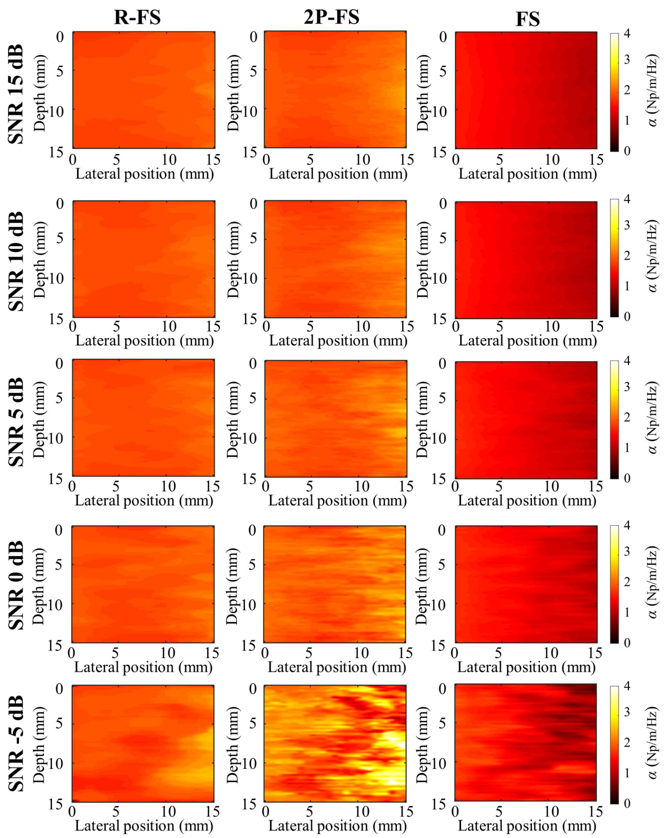

Fig. 7. Attenuation maps reconstructed for numerically simulated data with added noise (SNR of 15 to −5 dB) at a viscosity of 2 Pa·s for R-FS, 2P-FS, and FS imaging methods.

TABLE I

Mean (Np/m/Hz), SD, CV, and NRMSE of Computed Attenuation Coefficients on Numerically Simulated Data With Two Viscosities and Different SNRs

			SNR (dB)				
			15	10	5	0	-5
Viscosity: 0.5 Pa.s	Mean ± SD (CV, NRMSE (%))	**R-FS**	0.99 ± 0.04 (0.04,5.53)	0.99 ± 0.04 (0.04,6.16)	0.99 ± 0.04 (0.04,5.75)	0.99 ± 0.05 (0.05,6.19)	0.99 ± 0.08 (0.08,8.62)
		2P-FS	1.08 ± 0.06 (0.06,7.90)	1.08 ± 0.08 (0.07,8.69)	1.13 ± 0.08 (0.07,11.96)	1.18 ± 0.10 (0.09,17.82)	1.29 ± 0.17 (0.13,30.21)
		FS	0.71 ± 0.07 (0.1,31.71)	0.71 ± 0.07 (0.09,31.35)	0.74 ± 0.08 (0.11,29.48)	0.74 ± 0.08 (0.11,29.19)	0.77 ± 0.11 (0.15,27.70)
		AMUSE	0.99	0.98	0.97	1.01	1.09
		KV	1.03	1.03	1.03	1.03	1.03
Viscosity: 2 Pa.s	Mean ± SD (CV, NRMSE (%))	**R-FS**	1.92 ± 0.06 (0.03,6.59)	1.92 ± 0.07 (0.03,6.58)	1.93 ± 0.06 (0.03,6.45)	1.94 ± 0.08 (0.04,6.46)	1.97 ± 0.19 (0.10 ,10.09)
		2P-FS	1.97 ± 0.12 (0.06,6.78)	1.96 ± 0.12 (0.06,7.05)	2.01 ± 0.13 (0.06,6.54)	2.06 ± 0.16 (0.08,8.05)	2.22 ± 0.47 (0.21,24.67)
		FS	1.31 ± 0.12 (0.1,36.44)	1.31 ± 0.14 (0.11,36.61)	1.37 ± 0.18 (0.13,34.02)	1.36 ± 0.18 (0.13,34.33)	1.39 ± 0.31 (0.23,35.24)
		AMUSE	1.99	1.98	1.97	2.02	2.21
		KV	2.04	2.04	2.04	2.04	2.04

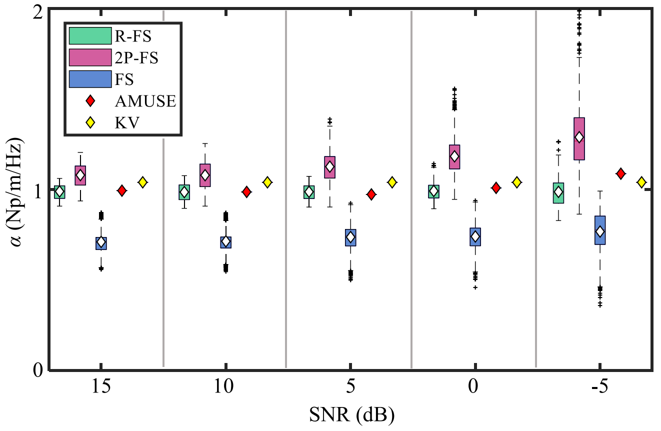

Fig. 8. Attenuation coefficients computed with R-FS, 2P-FS, FS, AMUSE, and KV ground truth methods for noisy simulations (SNR of 15 to −5 dB) at a viscosity of 0.5 Pa·s.

values close to the ground truth. Among image reconstruction methods, the proposed R-FS gave lowest biases, CVs, and NRMSEs compared with the KV model.

Another performance assessment was done by considering the ROI of Fig. 3(b) to be in line with the evaluation strategy of the 2P-FS method in [23]. Numerical simulations with the same viscosities as above and an SNR of −5 dB were used for results in Fig. 10. As mentioned earlier, 2P-FS considers only two spatial points in the lateral direction, whereas FS and R-FS can consider multiple spatial locations to improve the accuracy. The relation between attenuation and frequency obtained with AMUSE at both viscosities is displayed in Fig. 11. The slope of solid lines corresponds to attenuation coefficients given by this method at the focal depth of the radiation pressure push (1.10 Np/m/Hz at 0.5 Pa·s and 2.13 Np/m/Hz at 2 Pa·s). Fig. 12 illustrates comparative

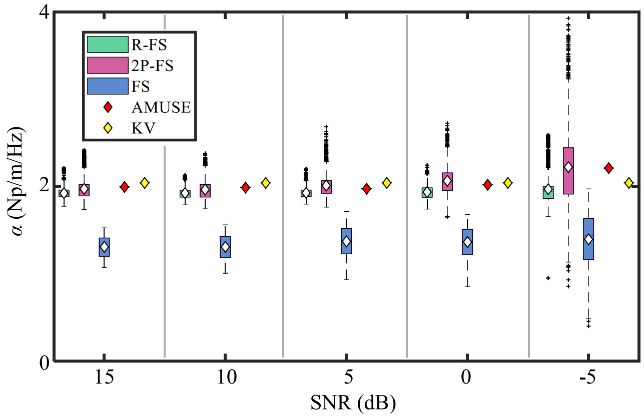

Fig. 9. Attenuation coefficients computed with R-FS, 2P-FS, FS, AMUSE, and KV ground truth methods for noisy simulations (SNR of 15 to −5 dB) at a viscosity of 2 Pa·s.

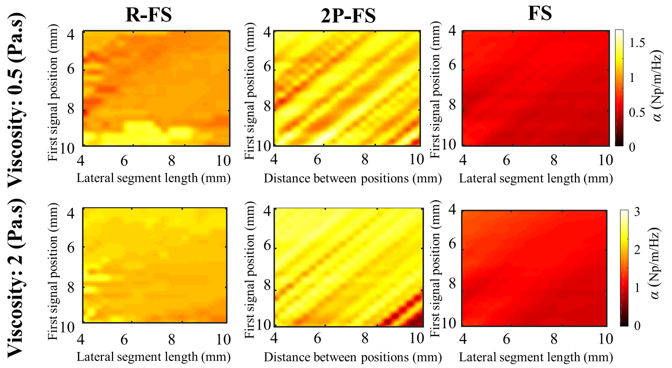

Fig. 10. Attenuation measurements for the numerically simulated data at an SNR of −5 dB and viscosities of 0.5 and 2 Pa·s, using R-FS, 2P-FS, and FS methods for different lateral positions at the focal depth.

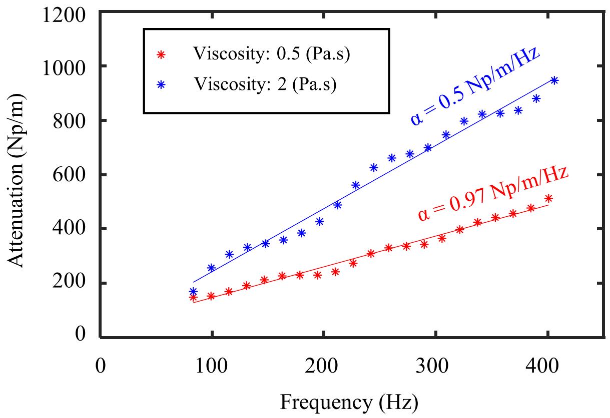

Fig. 11. Attenuation coefficients computation for the numerically simulated data by AMUSE at an SNR of −5 dB and viscosities of 0.5 and 2 Pa·s, for lateral measurements at the focal depth.

boxplots of attenuation coefficients averaged laterally at the focal depth. For other noisy simulation results with SNRs of 0, 5, 10, and 15 dB, see Supplementary materials (Section II). AMUSE provided results very close to the ground truth, and the proposed R-FS method provided the best performance in terms of bias and variability.

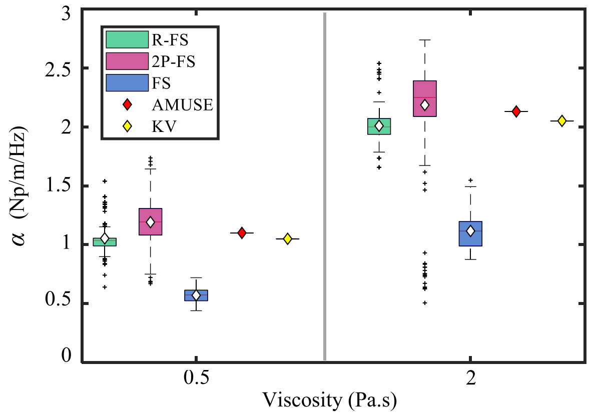

Fig. 12. Attenuation coefficients computed with R-FS, 2P-FS, FS, AMUSE, and KV ground truth methods for the numerically simulated data at an SNR of −5 dB and viscosities of 0.5 and 2 Pa·s.

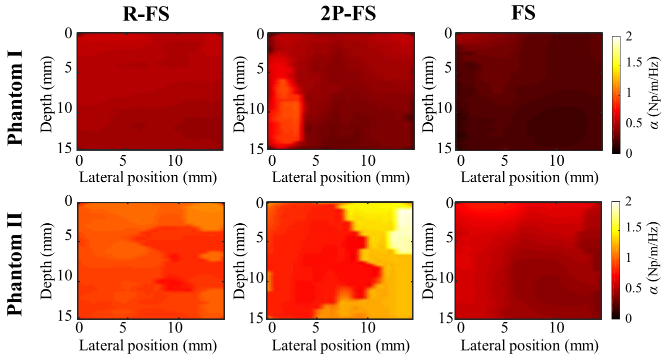

Fig. 13. Attenuation maps of homogeneous *in vitro* viscoelastic phantoms reconstructed with R-FS, 2P-FS, and FS methods.

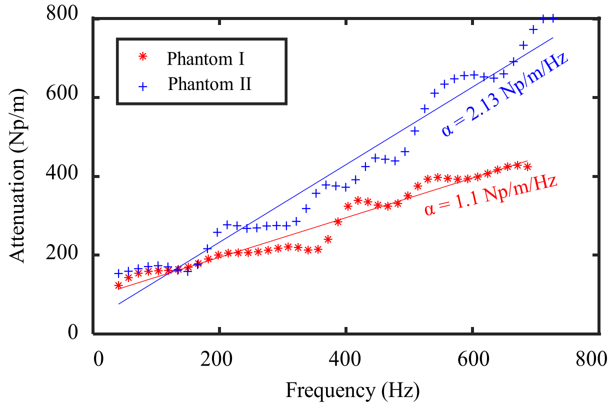

Fig. 14. Attenuation coefficients computation with AMUSE for both homogeneous *in vitro* viscoelastic phantoms.

B. In Vitro Phantoms

Fig. 13 presents reconstructed attenuation maps for two homogeneous phantoms in a rectangular ROI, as defined in Fig. 3(a). The phantom I was made with less xanthan gum than phantom II to have two levels of viscosity. Attenuation versus frequency plots estimated with the AMUSE method are presented in Fig. 14 along with their linear regressions. Fig. 15 presents boxplots of attenuation coefficients computed by R-FS, 2P-FS, FS, and AMUSE methods. Tabulated metrics are given in Table II.

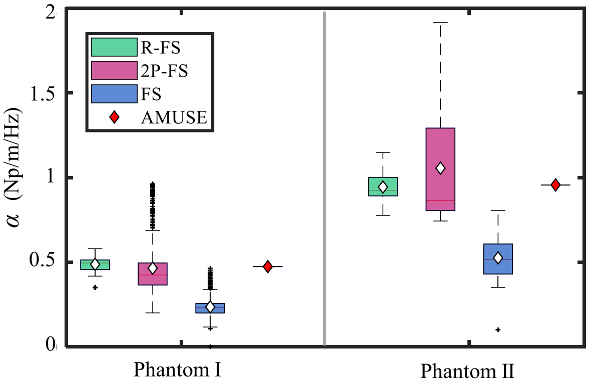

Fig. 15. Attenuation coefficients of homogeneous *in vitro* viscoelastic phantoms computed with R-FS, 2P-FS, FS, and AMUSE methods.

TABLE II
MEAN (NP/M/HZ), SD, AND CV OF ATTENUATION COEFFICIENTS WITHIN THE ROI FOR BOTH HOMOGENEOUS *In Vitro* VISCOELASTIC PHANTOMS

		Homogeneous *in vitro* phantoms	
		I	**II**
Mean ± SD (CV)	**R-FS**	0.49 ± 0.04 (0.08)	0.94 ± 0.07 (0.07)
	2P-FS	0.46 ± 0.17 (0.37)	1.06 ± 0.31 (0.29)
	FS	0.24 ± 0.05 (0.21)	0.53 ± 0.1 (0.19)
	AMUSE	0.50	0.97

As observed with simulations, FS and R-FS provided quite uniform attenuation maps, as expected for these homogeneous phantoms. Quantitatively, the proposed R-FS method gave closest results to AMUSE and minimum variability.

C. In Vivo Duck Livers

The liver region in three ducks scanned twice was manually selected by a veterinarian. After FF, histology analyses in all animals revealed a steatosis grade 3, no ballooning, inflammation grade 2, and fibrosis grade 1A [33]. Fig. 16 shows B-mode images and SW attenuation maps of duck livers before FF (i.e., reference state) reconstructed with R-FS, 2P-FS, and FS methods. Results after FF are given in Fig. 17. Higher SW attenuations are observed after FF, and nonhomogeneous displays are noticed (R-FS has lower variability). Attenuation versus frequency for AMUSE is presented in Fig. 18.

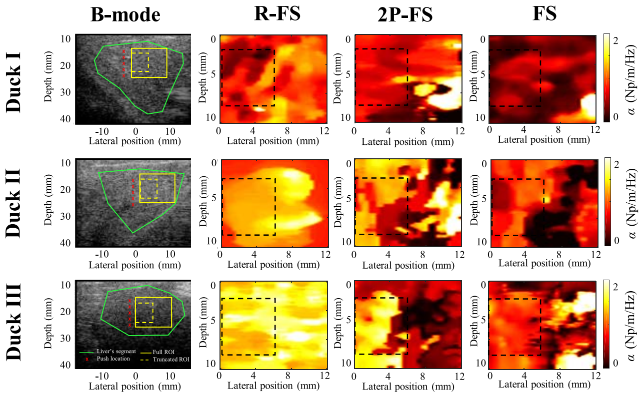

Fig. 16. B-mode images and attenuation maps of three *in vivo* duck livers before FF (reference state) assessed by R-FS, 2P-FS, and FS methods. Dashed line rectangles present the truncated ROI.

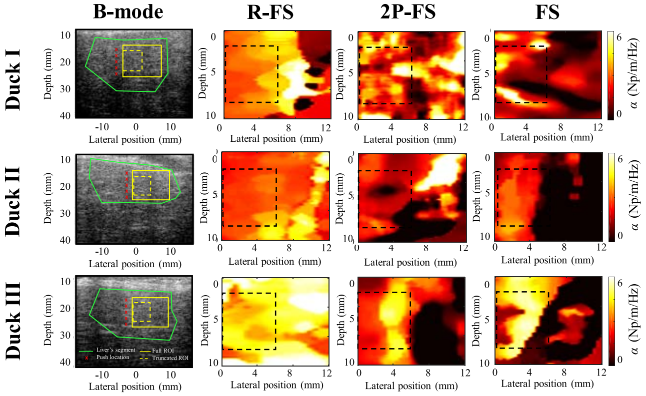

Fig. 17. B-mode images and attenuation maps of three *in vivo* duck livers after FF assessed by R-FS, 2P-FS, and FS methods. Dashed line rectangles present the truncated ROI.

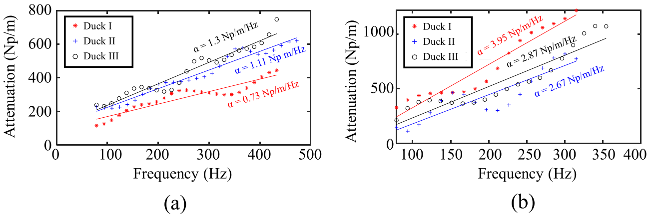

(a) (b)

Fig. 18. (a) Attenuation computation with AMUSE for three *in vivo* duck livers before FF; (b) Same display for three *in vivo* duck livers after FF.

Boxplot comparisons of methods are given in Fig. 19, and tabulated values are summarized in Table III. Truncated ROIs displayed in Figs. 16 and 17 (dashed line rectangles) were considered to evaluate the impact of distance with respect to push locations. For both truncated and full ROIs, the proposed R-FS imaging method provided closest results to the nonimaging AMUSE method. The SDs and CVs of R-FS were less than other methods for both ROIs (full and truncated). Based on Table III, SDs and CVs of all three methods providing attenuation maps were lower in truncated ROIs versus full ROIs.

V. DISCUSSION

This study aimed to propose improvements to FS (and 2P-FS) method for SW attenuation computation and to provide robust attenuation maps that could be utilized for medical diagnosis of steatotic livers. The R-FS, 2P-FS, and FS are based on fitting a gamma distribution to the amplitude spectrum. This is justified by the fact that the acoustic radiation pressure field excitation might not necessarily be in the form of a symmetric Gaussian shape in lossy *in vivo* media [5]. Thus, the Gaussian assumption is not necessarily valid and cannot be generalized. Interested readers may consult Bernard *et al.* [9]

TABLE III

MEAN (NP/M/HZ), SD, AND CV OF ATTENUATION COEFFICIENTS WITHIN TWO ROIs FOR THREE DUCK LIVERS BEFORE AND AFTER FF

		Duck I		Duck II		Duck III	
		Full ROI	Truncated ROI	Full ROI	Truncated ROI	Full ROI	Truncated ROI
Before FF Mean ± SD (CV)	**R-FS**	0.77 ± 0.51 (0.66)	0.66 ± 0.09 (0.14)	1.18 ± 0.26 (0.22)	1.16 ± 0.11 (0.09)	1.52 ± 0.22 (0.14)	1.47 ± 0.19 (0.13)
	2P-FS	0.86 ± 0.30 (0.35)	0.60 ± 0.21 (0.35)	0.92 ± 0.55 (0.60)	1.03 ± 0.27 (0.26)	0.73 ± 0.54 (0.74)	1.36 ± 0.32 (0.24)
	FS	0.47 ± 0.48 (1.02)	0.37 ± 0.17 (0.46)	0.50 ± 0.53 (1.06)	0.72 ± 0.22 (0.31)	0.85 ± 0.61 (0.72)	0.91 ± 0.14 (0.15)
	AMUSE	0.73		1.11		1.3	
After FF Mean ± SD (CV)	**R-FS**	3.13 ± 1.73 (0.55)	3.11 ± 0.31 (0.10)	3.16 ± 0.76 (0.24)	2.63 ± 0.19 (0.07)	4.84 ± 1.13 (0.23)	4.12 ± 0.62 (0.15)
	2P-FS	2.92 ± 1.74 (0.60)	2.89 ± 1.05 (0.36)	0.55 ± 1.86 (3.38)	2.54 ± 0.51 (0.20)	1.63 ± 2.45 (1.50)	3.85 ± 1.59 (0.41)
	FS	1.50 ± 1.55 (1.03)	2.15 ± 1.35 (0.63)	1.56 ± 3.18 (2.04)	1.74 ± 0.71 (0.41)	1.40 ± 2.55 (1.82)	3.14 ± 1.02 (0.32)
	AMUSE	2.87		2.67		3.95	

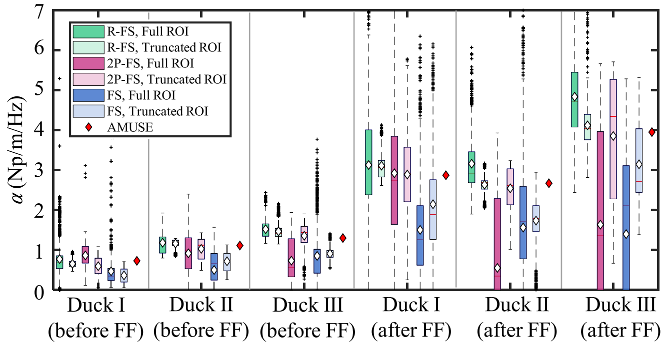

Fig. 19. Attenuation coefficients for *in vivo* duck livers computed with R-FS, 2P-FS, FS, and AMUSE methods. Two ROIs are considered here.

for a detailed justification for choosing a gamma fit for SW data acquired in lossy media. In this work, a Gaussian-shaped force was considered to produce SWs in the simulations. See Appendix A for a description of the relation between the Gaussian source and the approximation of the SW field with a gamma distribution.

Two main improvements were applied to the FS method; first, the shape parameter of the gamma frequency fit on the SW attenuation spectrum was not assumed constant and equal to the shape parameter of the source spectrum. This assumption is supported by Fig. 4, where it can be noticed that the shape parameter varies with lateral distance. This modification of a nonconstant shape parameter yielded high R-squared values of gamma fits, increasing the confidence in this model. The second modification was to use an A-RANSAC line fitting approach to further improve robustness in the presence of outliers. Outliers may appear due to tissue heterogeneity related to boundary effects, air pockets when performing gel phantom experiments, or from the measurement noise. The A-RANSAC method is able to automatically define a threshold based on each dataset (according to its inliers) to reject corrupted measures. This novelty allowed superior results with the proposed method when compared with the FS or 2P-FS method. Other line fitting techniques (e.g., LLSQ and Robust-fit) are assuming that the maximum deviation of a data point is a function of the size of the dataset and that there are always a large enough number of good values to smooth out any outliers. The A-RANSAC algorithm was capable of rejecting such outliers and, thus, could be used in the context of this study for smoothing data that could contain a significant percentage of outliers (e.g., in the case of highly attenuating steatotic duck livers).

One of the main objectives of this work was to reconstruct an attenuation map of a ROI inside a medium for diagnostic applications. This is specifically important for investigating the tissue texture that may arise due to fat deposition [26]. Most studies in elastography consider the assumption of a homogeneous medium to compute SW parameters. The proposed study reported a comprehensive comparative analysis of R-FS, 2P-FS, and FS methods for SW attenuation map reconstructions in homogeneous but also heterogeneous (*in vivo*) situations, while considering the model's ability to produce low biases and low variances in the case of R-FS, thanks to the outlier rejection strategy adopted in this work. Clearly, R-FS was successful in obtaining attenuation maps with less biases and variances than other imaging methods. Furthermore, two additional quantitative methods, AMUSE and the KV model in the case of simulations (ground truth), were utilized to validate observed findings. Numerical phantoms are ideal for a comprehensive analysis as they can provide ground truth estimates and simulations of noisy conditions. In the case of *in vitro* and *in vivo* datasets where ground truths were not available, the AMUSE model was considered as the reference method.

Simulation results of Figs. 8 and 9 revealed that FS and R-FS attenuation maps were smoother than 2P-FS maps in the presence of noise (especially at the SNR of −5 dB). This is because several spatial data points (compared with two points for 2P-FS) were considered in the lateral direction [23]. However, FS underestimated attenuation coefficients due to its assumption of a constant shape parameter at any location [9]. The proposed R-FS model overcame limitations of other imaging methods and, thus, provided robust estimation of the attenuation coefficient. This was validated by comparing results with KV and AMUSE estimates. The ROI selection was consistent among methods in this study to obtain comparative results. In our previous study with the FS model, one had to select the ROI location at different positions to minimize the impact of noisy wave fields [9], [33]. Consequently, SW attenuation values may differ at the end of the FF process between studies.

Figs. 10 and 11 reported a sensitivity analysis of attenuation computations over a line at the focal depth. Different first signal positions and varying lateral segments were considered for numerically simulated data at an SNR of −5 dB. These maps were provided to compare our results with similar maps reported for the 2P-FS method [23]. Our results are in line with previous statements, as R-FS had less variation and closer mean values to the ground truth, especially in the case of noisy datasets.

In vitro phantom and *in vivo* duck liver datasets confirmed predictions made using simulations. Indeed, the R-FS method outperformed other imaging methods and provided estimates closer to AMUSE. As displayed with fatty duck liver datasets, selecting a ROI closer to the radiation pressure source improved SW attenuation estimates because of a higher SNR attributed to the enhanced attenuation with distance [9]. For both truncated and full ROIs, the proposed R-FS algorithm again provided the best performance. The use of a varying shape parameter and the A-RANSAC line fitting allowed such improvements over FS and 2P-FS methods.

Limitations of the proposed model are that all FS methods are inherently based on the assumption of locally isotropic and homogeneous media. Furthermore, it is also assumed that attenuation depends linearly on SW frequency, which may not hold for some biological tissues [37]–[40]. Indeed, nonlinear frequency dispersion behaviors have been reported for bovine *ex vivo* muscles [41], mammalian soft tissues [42], human breasts [43], and livers [44], [45]. Moreover, for fatty liver tissues at high frequencies (≥1000 Hz), SW attenuation has also been shown to display a nonlinear relationship with frequency [44], [46].

Future studies should aim validating this model with *in vivo* human data, which may be more challenging especially in obese patients. The hypothesis of locally isotropic and homogeneous tissues may reveal an enhanced variability in the case of mechanical heterogeneities, such as cancer tumors within the liver parenchyma. Notice that AMUSE is also limited by the assumption of an isotropic and homogeneous tissue, and it does not provide images of SW attenuation. Future validations should, thus, be done to better appreciate limitations of the R-FS imaging method in the case of anisotropy and/or tissue heterogeneity. Results on *in vivo* fatty duck livers nevertheless allowed appreciating the robustness of R-FS for displaying SW attenuation heterogeneities attributed to the presence of fatty vacuoles.

VI. CONCLUSION

The R-FS method for SW attenuation coefficient computation was developed based on varying gamma fitting shape and rate parameters and by using an A-RANSAC line-fitting method. The proposed imaging method was tested on noisy simulation data, homogeneous phantoms, and *in vivo* duck livers without or with fat depositions. A comprehensive comparison with FS and 2P-FS methods suggested that the proposed R-FS algorithm is offering a robust approach to compute the attenuation coefficient. This imaging method also compared favorably with the numerically simulated ground truth SW attenuation measures and to the AMUSE algorithm. We envision that R-FS improvements may lead to accurate imaging of viscoelasticity in biological tissues, which may provide robust biomarkers of human fatty livers for diagnosis or of other liver or organ pathologies.

APPENDIX A

Here, the theory supporting the relation between the Gaussian source and the approximation of the SW field with a gamma distribution is presented. Using the notation from [47] in cylindrical coordinates and [31, eq. 1], the governing equation of the SW motion produced by a body force excitation can be written as

$$\nabla^2 u_z - \frac{1}{c^2}\frac{\partial^2 u_z}{\partial t^2} = -\frac{1}{c^2} F_z g(t) \tag{A-1}$$

where ∇^2 is the Laplacian operator in cylindrical coordinates, u_z is the displacement of the SW in the z-direction of cylindrical coordinates [u_z is a function of both location (r, θ, z) and time (t)], c is the velocity of the wave, F_z is the distribution of the applied body force in the z-direction, and $g(t)$ is the temporal application of the force.

In the case of our simulations, we selected F_z with a Gaussian shape

$$F_z(r) = A_0 \left(\frac{1}{2\sigma^2}\right) e^{-\left(\frac{r}{2\sigma}\right)^2} \tag{A-2}$$

where r is the cylindrical radius, A_0 is the force intensity, and σ^2 is half the variance of the pulse shape. Applying the constraint of initial conditions to be zero velocity and zero displacement, (A-1) can be rewritten as

$$\nabla^2 u_z(r,t) - \frac{1}{c^2}\frac{\partial^2 u_z(r,t)}{\partial t^2} = -\frac{1}{c^2} F_z(r) g(t). \tag{A-3}$$

Assuming a viscoelastic medium according to [31] and taking the temporal Fourier transform of (A-3) yields

$$\nabla^2 U_z(r,\omega) - \frac{\omega^2}{\hat{c}(\omega)^2} U_z(r,\omega) = -\frac{1}{\hat{c}(\omega)^2} F_z(r) G(\omega) \tag{A-4}$$

where $U_z(r,\omega)$ and $G(\omega)$ are temporal Fourier transforms of $u_z(r,t)$ and $g(t)$, respectively, ω is the angular frequency with respect to time, $\hat{c}(\omega)$ represents the SW velocity in the viscoelastic medium with shear storage $\mu_s(\omega)$ and loss $\mu_l(\omega)$ moduli, and mass density ρ. With above definitions, $\hat{c}(\omega) = (\hat{\mu}/\rho)^{1/2}$, where $\hat{\mu} = \mu_s(\omega) + i\mu_l(\omega)$.

According to [31] and by applying the zeroth-order Hankel transform $(\mathcal{H}_0)$ in space to (A-4) in cylindrical coordinates yields

$$\hat{U}_z(\varepsilon,\omega) = \frac{\hat{k}^2}{\omega^2}\frac{\hat{F}_z(\varepsilon)\, G(\omega)}{\varepsilon^2 - \hat{k}^2}. \tag{A-5}$$

where $\hat{U}_z(\varepsilon,\omega)$ is the Hankel transform of $U_z(r,\omega)$, ε is the spatial frequency, $\hat{k}$ is the complex wavenumber $\hat{k} = \omega/\hat{c}(\omega)$, and $\hat{F}_z(\varepsilon)$ is the Hankel transform of $F_z(r)$. By assuming a force as in (A-2), and using the identity $\mathcal{H}\{e^{-(1/2)a^2r^2}\} = (1/a^2)e^{-(r^2/2a^2)}$, then by setting $a^2 = (1/(2\sigma^2))$, $\hat{F}_z(\varepsilon)$ can be computed as

$$\hat{F}_z(\varepsilon) = A_0\, e^{-\sigma^2-\varepsilon^2}. \tag{A-6}$$

Now, by applying the inverse Hankel transform to $\hat{U}_z(\varepsilon,\omega)$ in (A-5), one may write $U_z(r,\omega)$ as follows:

$$U_z(r,\omega) = \frac{\hat{k}^2}{\omega^2}\int_0^\infty \frac{\hat{F}_z(\varepsilon)\, G(\omega)}{\varepsilon^2 - \hat{k}^2} J_0(\varepsilon r)\, \varepsilon d\varepsilon \tag{A-7}$$

where J_o is the zero-order Bessel function. One may factor out $G(\omega)$ in (A-7), which gives

$$U_z(r,\omega) = \frac{\hat{k}^2\, G(\omega)}{\omega^2}\int_0^\infty \frac{\hat{F}_z(\varepsilon)}{\varepsilon^2 - \hat{k}^2} J_0(\varepsilon r)\, \varepsilon d\varepsilon. \tag{A-8}$$

Using Baddour's theorem 4 [48] for complex wave numbers along with (A-8), one may solve for $U_z(r,\omega)$

$$U_z(r,\omega) = -G(\omega)\frac{\hat{k}^2}{\omega^2}\frac{\pi i}{2}H_0^{(2)}\left(\hat{k}\,r\right)\hat{F}_z\left(\hat{k}\right) \tag{A-9}$$

where $H_0^{(2)}$ is the Hankel function of the second kind, and $\hat{k}$ is a complex number, with a negative imaginary part of the form $\hat{k} = (\omega/\tilde{c}) - i\alpha_1\omega$, where α_1 is the first order Taylor approximation of the attenuation, and where in a dispersive medium: $\tilde{c} = c_0 + c_1\omega$. Substituting (A-6) into (A-9) then yields

$$U_z(r,\omega) = -G(\omega)\frac{\hat{k}^2}{\omega^2}A_0\frac{\pi i}{2}H_0^{(2)}\left(\hat{k}\,r\right)e^{-\sigma^2\left(\hat{k}^2\right)}. \tag{A-10}$$

Substituting the expression for $\hat{k}$ into (A-10) yields

$$\begin{aligned} U_z(r,\omega) &\\ &= -G(\omega)\frac{\left(\frac{\omega}{\tilde{c}} - i\alpha_1\omega\right)^2}{\omega^2}A_0\frac{\pi\, i}{2}H_0^{(2)}\left(\left(\frac{\omega}{\tilde{c}} - i\alpha_1\omega\right)r\right)\\ &\quad\times e^{-\sigma^2\left(\left(\frac{\omega}{\tilde{c}} - i\,\alpha_1\,\omega\right)^2\right)}. \end{aligned} \tag{A-11}$$

Assuming a complex number of the form $z = x + i\,y$, where $0 < y \ll x$, an approximation is suggested in [49] as follows:

$$H_0^{(2)}(x - i\,y) \cong e^{-y}H_0^{(2)}(x). \tag{A-12}$$

Now, by assuming $0 < \alpha_1 \ll (1/\tilde{c})$ and considering (A-11) and (A-12), one obtains the approximation

$$U_z(r,\omega) \cong -G(\omega)\left(\frac{1}{\tilde{c}}\right)^2 A_0\frac{\pi i}{2}e^{-\alpha_1\omega r}H_0^{(2)}\left(\frac{\omega}{\tilde{c}}r\right)e^{-\sigma^2\left(\frac{\omega}{\tilde{c}}\right)^2}. \tag{A-13}$$

By inserting the assumption for a dispersive medium, $U_z(r,\omega)$ can be expressed as follows:

$$\begin{aligned} U_z(r,\omega) &\\ &\cong -G(\omega)\left(\frac{1}{c_0 + c_1\omega}\right)^2 A_0\frac{\pi i}{2}e^{-\alpha_1\omega r}H_0^{(2)}\left(\frac{\omega}{c_0 + c_1\omega}r\right)\\ &\quad\times e^{-\sigma^2\left(\frac{\omega}{c_0 + c_1\omega}\right)^2} \end{aligned} \tag{A-14}$$

and by considering a small dispersion ($c_1 \approx 0$) for the sake of simplicity, one reaches

$$U_z(r,\omega) \cong -G(\omega)\left(\frac{1}{c_0}\right)^2 A_0\frac{\pi i}{2}e^{-\alpha_1\omega r}H_0^{(2)}\left(\frac{\omega}{c_0}r\right)e^{-\sigma^2\left(\frac{\omega}{c_0}\right)^2}. \tag{A-15}$$

One may then write $V_z(r,\omega) = i\omega\, U_z(r,\omega)$ as follows:

$$V_z(r,\omega) \cong G(\omega)\left(\frac{1}{c_0}\right)^2 A_0\,\omega\,\frac{\pi}{2}e^{-\alpha_1\omega r}H_0^{(2)}\left(\frac{\omega}{c_0}r\right)e^{-\sigma^2\left(\frac{\omega}{c_0}\right)^2}. \tag{A-16}$$

According to [47, eq. 42], the Hankel function $H_0^{(2)}((\omega/c_0)r)$ may be replaced by the approximation

$$H_0^{(2)}\left(\frac{\omega}{c_0}r\right) \cong \sqrt{\frac{2}{\pi\left(\frac{\omega}{c_0}r\right)}}\,e^{-i\left(\frac{\omega}{c_0}r - \frac{\pi}{4}\right)}. \tag{A-17}$$

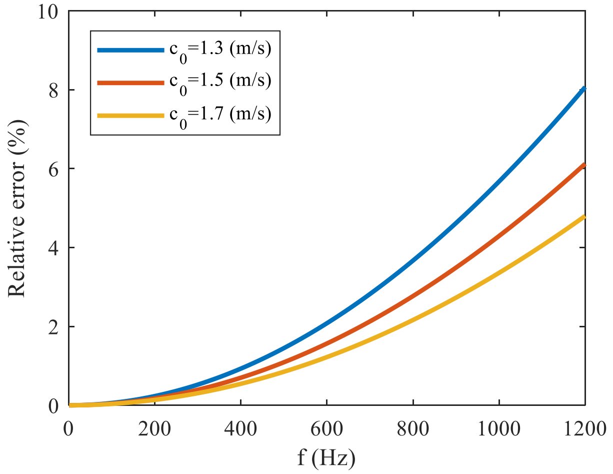

Fig. 20. Relative error (%) as a function of f (Hz) for three values of c_0 (m/s).

Therefore, one obtains the approximation

$$\begin{aligned} V_z(r,\omega) &\\ &\cong G(\omega)\left(\frac{1}{c_0}\right)^2 A_0\,\omega\,\frac{\pi}{2}e^{-\alpha_1\omega r}\sqrt{\frac{2}{\pi\left(\frac{\omega}{c_0}r\right)}}\\ &\quad\times e^{-i\left(\frac{\omega}{c_0}r - \frac{\pi}{4}\right)}e^{-\sigma^2\left(\frac{\omega}{c_0}\right)^2}. \end{aligned} \tag{A-18}$$

In our finite-element simulations, following [31], $g(t)$ is a temporal rectangular pulse of the form $g(t) = \mathrm{rect}((t/\tau) - (1/2))$, where $\tau = 1$ (ms), which yields:

$$G(\omega) = \frac{1}{\sqrt{\frac{2\pi}{\tau^2}}}\mathrm{sinc}\frac{\omega}{\frac{2\pi}{\tau^2}}e^{-\frac{i}{2}\omega}. \tag{A-19}$$

Substituting (A-19) into (A-18) yields

$$\begin{aligned} V_z(r,\omega) \cong{}& \frac{1}{\sqrt{\frac{2\pi}{\tau^2}}}\,\mathrm{sinc}\frac{\omega}{\frac{2\pi}{\tau^2}}\left(\frac{1}{c_0}\right)^2 A_0\,\omega\,\frac{\pi}{2}\sqrt{\frac{2}{\pi\left(\frac{\omega}{c_0}r\right)}}\\ &\times e^{-i\left(\left(\frac{r}{c_0} + \frac{1}{2}\right)\omega - \frac{\pi}{4}\right)}e^{-\left(\sigma^2\left(\frac{\omega}{c_0}\right)^2 + \alpha_1\omega r\right)}. \end{aligned} \tag{A-20}$$

Equation (A-20) may be simplified by applying further approximations. In the range of angular frequencies $0 < \omega \leq (2\pi \times 1200)$ rad/s, by setting $\sigma = 5 \times 10^{-5}$ m and $c_0 = 1.7$ m/s (based on our simulations), one may assume that $\sigma^2((\omega/c_0))^2 \leq (((0.05 \times 2\pi \times 1.2)/1.7))^2 \approx 0.049$, so that $|e^{-\sigma^2((\omega/c_0))^2} - 1| \leq 0.048$. Thus, we can neglect the factor $e^{-\sigma^2((\omega/c_0))^2}$ in (A-20), with a relative error of at most 4.8%.

Fig. 20 displays relative errors for different values of f and c_0 (based on the simulations of this work and the literature [50], [51]), which supports the approximation of $e^{-\sigma^2((\omega/c_0))^2} \approx 1$. Thus, we can approximate (A-20) with

$$V_z(r,\omega) \cong A(r,\omega)\,e^{-i\left(\left(\frac{r}{c_0} + \frac{1}{2}\right)\omega - \frac{\pi}{4}\right)}e^{-(\alpha_1\omega r)} \tag{A-21}$$

where

$$A(r,\omega) = \frac{1}{\sqrt{\frac{2\pi}{\tau^2}}}\mathrm{sinc}\frac{\omega}{\frac{2\pi}{\tau^2}}\left(\frac{1}{c_0}\right)^2 A_0\,\omega\,\frac{\pi}{2}\sqrt{\frac{2}{\pi\left(\frac{\omega}{c_0}r\right)}}. \tag{A-22}$$

Next, one may write (A-22) as follows:

$$A(r,\omega) \cong A_1(r)\ A_2(\omega) \tag{A-23}$$

where $A_1(r) \cong (1/\sqrt{r})(1/(((2\pi/\tau^2))^{1/2}))((1/c_0))^2 A_0 (((\pi c_0)/2))^{1/2}$ and $A_2(\omega) \cong \operatorname{sinc}(\omega/((2\pi/\tau^2)))\sqrt{\omega}$. Equation (A-23) simplifies to

$$A(r,\omega) \cong A_1(r)\ \omega^{n-1} \tag{A-24}$$

where the exponent n is around 1.5. This value might be slightly lower or higher due to the oscillatory property of the sinc function and the approximations used to derive the equations.

Using the above approximations, (A-21) can be simplified in the form of a gamma distribution (up to a constant factor); therefore, the amplitude spectrum can be expressed as follows:

$$|S(r,\omega)| \propto A(r)\,\omega^{n-1}\,e^{-\beta(r)\omega} \tag{A-25}$$

where $\beta(r) = \alpha_1 r$.

Furthermore, as an example of an excitation's shape other than the Gaussian one, Parker and Baddour [47] derived, under the assumption of a "bell shape" beam [47, eq. 33] in a dispersive medium together with the other assumptions provided in [47], that the particle velocity in the axial (z) direction can be expressed as follows:

$$V_z(r,\omega) \cong A_0 \frac{\pi}{2}\omega\, H_0^{(2)}\left(\frac{\omega}{c_0} r - i\alpha_1\omega r\right)\frac{e^{-a\left(\frac{\omega}{c_0}\right)}}{\frac{\omega}{c_0}} \tag{A-26}$$

where a is a beamwidth parameter. According to (A-12) and (A-17), one may recast (A-26) as follows:

$$V_z(r,\omega) \cong A_0 \frac{\pi}{2}\omega\, e^{-(\alpha_1\omega r)}\sqrt{\frac{2}{\pi\left(\frac{\omega}{c_0} r\right)}}\, e^{-i\left(\frac{\omega r}{c_0} - \frac{\pi}{4}\right)}\frac{e^{-a\left(\frac{\omega}{c_0}\right)}}{\frac{\omega}{c_0}}. \tag{A-27}$$

It follows that the amplitude spectrum can be expressed in the form of a gamma distribution, up to a constant of proportionality:

$$|S(r,\omega)| \propto A(r)\,\omega^{n-1}\,e^{-\beta(r)\omega} \tag{A-28}$$

upon setting $n = 0.5$, $A(r) = A_0(((\pi c_0^3)/2r))^{1/2}$, and $\beta(r) = (a/c_0) + \alpha_1 r$.

Altogether, whether one adopts a Gaussian shape (with sufficiently small σ) or a modified bell shape according to [47, eq. 33], then one obtains a gamma distribution within reasonable approximation. Based on the above arguments, we think that our assumption is quite reasonable to fit the SW amplitude spectrum with a gamma distribution (up to a constant factor). As an alternative approach for SW motion with a localized excitation force [19], the equation of motion can be differentiated into inside and outside of a maximum source radius (R). By neglecting the force outside of R, the equation of motion can also be written in [19, eq. 27], which is similar to [47]. Using the same approach as described in this appendix, one can reach to the gamma distribution for the SW motion.

TABLE IV

ESTIMATED SNRS FOR SIMULATIONS, AND *IN VITRO* AND *IN VIVO* EXPERIMENTS. SD, STANDARD DEVIATION; FF, FORCE FEEDING

Simulation viscosity 0.5 Pa·s		Simulation viscosity 2 Pa·s	
Name	Estimated SNR (dB) Mean±SD	Name	Estimated SNR (dB) Mean±SD
SNR 15	11.11 ± 3.53	SNR 15	11.67 ± 3.85
SNR 10	8.72 ± 2.84	SNR 10	8.93 ± 2.92
SNR 5	4.90 ± 1.91	SNR 5	4.89 ± 1.81
SNR 0	0.08 ± 1.04	SNR 0	-0.02 ± 0.91
SNR -5	-5.27 ± 0.48	SNR -5	-5.41 ± 0.43

In vitro phantom		*In vivo* data		
Name	Estimated SNR (dB) Mean±SD		Name	Estimated SNR (dB) Mean±SD
Phantom I	5.96 ± 3.24	Before FF	Duck I	-4.91 ± 4.48
Phantom II	1.41 ± 4.17		Duck II	9.87 ± 4.24
			Duck III	-6.55 ± 2.56
		After FF	Duck I	8.46 ± 4.63
			Duck II	1.62 ± 7.44
			Duck III	-0.53 ± 3.36

APPENDIX B

The SNR for simulations, and *in vitro* and *in vivo* experiments were estimated using the following equation inspired from [52]:

$$\mathrm{SNR} = \frac{\mu^2}{\mathrm{MSE}} \text{ and } \mathrm{MSE} = E\left[\left(d_\mathrm{e} - d_\mathrm{g}\right)^2\right] \tag{B-1}$$

where μ is the mean displacement value at a specific axial location, MSE is the mean square error, d_e is the estimated displacement value, and d_g is the "predicted" ground truth value. For experimental data, d_g is unknown, so we have assumed that it is equal to the mean value of all axial locations within the ROI, which is a common assumption in the literature [53], [54]. Such an approach decreases the variance but has little impact on the bias. A median filter was also applied on the mean value of all axial locations to further reduce the variance of the estimated mean, and get closer to a ground truth. The same approach was done for both simulation and experimental data, even if the true SNR was known with simulations. The objective here was to verify if the estimated SNR with (B-1) would be close to the imposed one obtained by adding noise on simulated data, which would validate *in vitro* and *in vivo* computations. All SNR estimations are provided in Table IV. For SNR approximations versus time figures, please see Supplementary materials (Section III).

ACKNOWLEDGMENT

The authors thank Fernande Ouellet and Francis Laroche (farm “Rusé comme un canard,” Granby, QC, Canada); Nathalie Vermette, veterinarian, for acquiring ultrasound recordings on living awake ducks at the farm; and Dr. François Destrempes for his assistance in Appendix A of this work.

REFERENCES

[1] M. M. Doyley and K. J. Parker, “Elastography: General principles and clincial applications,” *Ultrasound Clinics*, vol. 9, no. 1, pp. 1–11, Jan. 2014.

[2] J. L. Gennisson *et al.*, “Ultrasound elastography: Principles and techniques,” *Diagn Interv Imag.*, vol. 94, no. 5, pp. 487–495, May 2013.

[3] A. Tang, G. Cloutier, N. M. Szeverenyi, and C. B. Sirlin, “Ultrasound elastography and MR elastography for assessing liver fibrosis: Part 1, principles and techniques,” *Amer. J. Roentgenol.*, vol. 205, no. 1, pp. 22–32, 2015.

[4] A. Tang, G. Cloutier, N. M. Szeverenyi, and C. B. Sirlin, “Ultrasound elastography and MR elastography for assessing liver fibrosis: Part 2, diagnostic performance, confounders, and future directions,” *Amer. J. Roentgenol.*, vol. 205, no. 1, pp. 33–40, Jul. 2015.

[5] K. Nightingale, “Acoustic radiation force impulse (ARFI) imaging: A review,” *Current Med. Imag. Rev.*, vol. 7, no. 4, pp. 328–339, Nov. 2011.

[6] M. Friedrich-Rust *et al.*, “Liver fibrosis in viral hepatitis: Noninvasive assessment with acoustic radiation force impulse imaging versus transient elastography,” *Radiology*, vol. 252, no. 2, pp. 595–604, 2009.

[7] M. Muller *et al.*, “Quantitative viscoelasticity mapping of human liver using supersonic shear imaging: Preliminary *in vivo* feasability study,” *Ultrasound Med. Biol.*, vol. 35, no. 2, pp. 219–229, Feb. 2009.

[8] M. Tanter *et al.*, “Quantitative assessment of breast lesion viscoelasticity: Initial clinical results using supersonic shear imaging,” *Ultrasound Med. Biol.*, vol. 34, no. 9, pp. 1373–1386, Sep. 2008.

[9] S. Bernard, S. Kazemirad, and G. Cloutier, “A frequency-shift method to measure shear-wave attenuation in soft tissues,” *IEEE Trans. Ultrason., Ferroelectr., Freq. Control*, vol. 64, no. 3, pp. 514–524, Mar. 2017.

[10] I. Z. Nenadic *et al.*, “Attenuation measuring ultrasound shearwave elastography and *in vivo* application in post-transplant liver patients,” *Phys. Med. Biol.*, vol. 62, no. 2, pp. 484–500, Jan. 2017.

[11] A. K. Sharma *et al.*, “Attenuation of shear waves in normal and steatotic livers,” *Ultrasound Med. Biol.*, vol. 45, no. 4, pp. 895–901, Apr. 2019.

[12] H. Li *et al.*, “Viscoelasticity imaging of biological tissues and single cells using shear wave propagation,” *Frontiers Phys.*, vol. 9, no. 350, pp. 1–39, Jun. 2021.

[13] C. T. Barry *et al.*, “Shear wave dispersion measures liver steatosis,” *Ultrasound Med. Biol.*, vol. 38, no. 2, pp. 175–182, Feb. 2012.

[14] C. T. Barry *et al.*, “Mouse liver dispersion for the diagnosis of early-stage fatty liver disease: A 70-sample study,” *Ultrasound Med. Biol.*, vol. 40, no. 4, pp. 704–713, Apr. 2014.

[15] S. Chen, M. Fatemi, and J. F. Greenleaf, “Quantifying elasticity and viscosity from measurement of shear wave speed dispersion,” *J. Acoust. Soc. Amer.*, vol. 115, no. 6, pp. 2781–2785, Jun. 2004.

[16] T. Deffieux *et al.*, “Shear wave spectroscopy for *in vivo* quantification of human soft tissues visco-elasticity,” *IEEE Trans. Med. Imag.*, vol. 28, no. 3, pp. 313–322, Mar. 2009.

[17] S. Kazemirad, S. Bernard, S. Hybois, A. Tang, and G. Cloutier, “Ultrasound shear wave viscoelastography: Model-independent quantification of the complex shear modulus,” *IEEE Trans. Ultrason., Ferroelectr., Freq. Control*, vol. 63, no. 9, pp. 1399–1408, Sep. 2016.

[18] E. Budelli *et al.*, “A diffraction correction for storage and loss moduli imaging using radiation force based elastography,” *Phys. Med. Biol.*, vol. 62, no. 1, pp. 91–106, Jan. 2017.

[19] N. C. Rouze, Y. Deng, C. A. Trutna, M. L. Palmeri, and K. R. Nightingale, “Characterization of viscoelastic materials using group shear wave speeds,” *IEEE Trans. Ultrason., Ferroelectr., Freq. Control*, vol. 65, no. 5, pp. 780–794, May 2018.

[20] C. A. Trutna, N. C. Rouze, M. L. Palmeri, and K. R. Nightingale, “Measurement of viscoelastic material model parameters using fractional derivative group shear wave speeds in simulation and phantom data,” *IEEE Trans. Ultrason., Ferroelectr., Freq. Control*, vol. 67, no. 2, pp. 286–295, Feb. 2020.

[21] J. Ormachea and K. J. Parker, “Reverberant shear wave phase gradients for elastography,” *Phys. Med. Biol.*, vol. 66, no. 17, Aug. 2021, Art. no. 175001.

[22] N. C. Rouze, M. L. Palmeri, and K. R. Nightingale, “An analytic, Fourier domain description of shear wave propagation in a viscoelastic medium using asymmetric Gaussian sources,” *J. Acoust. Soc. Amer.*, vol. 138, no. 2, pp. 1012–1022, Aug. 2015.

[23] P. Kijanka and M. W. Urban, “Two-point frequency shift method for shear wave attenuation measurement,” *IEEE Trans. Ultrason., Ferroelectr., Freq. Control*, vol. 67, no. 3, pp. 483–496, Mar. 2020.

[24] L. Yazdani, M. Bhatt, G. Bosio, and G. Cloutier, “Improved frequency-shift method for shear wave attenuation computation,” in *Proc. IEEE Int. Ultrason. Symp. (IUS)*, Sep. 2020, pp. 1–4.

[25] M. A. Fischler and R. Bolles, “Random sample consensus: A paradigm for model fitting with applications to image analysis and automated cartography,” *Commun. ACM*, vol. 24, no. 6, pp. 381–395, 1981.

[26] M. Bhatt *et al.*, “Reconstruction of viscosity maps in ultrasound shear wave elastography,” *IEEE Trans. Ultrason., Ferroelectr., Freq. Control*, vol. 66, no. 6, pp. 1065–1078, Apr. 2019.

[27] M. H. Wang *et al.*, “Improving the robustness of time-of-flight based shear wave speed reconstruction methods using RANSAC in human liver *in vivo*,” *Ultrasound Med. Biol.*, vol. 36, no. 5, pp. 802–813, May 2010.

[28] M. Waine, C. Rossa, R. Sloboda, N. Usmani, and M. Tavakoli, “3D shape visualization of curved needles in tissue from 2D ultrasound images using RANSAC,” in *Proc. IEEE Int. Conf. Robot. Autom. (ICRA)*, May 2015, pp. 4723–4728.

[29] Y. Zhao, Y. Shen, A. Bernard, C. Cachard, and H. Liebgott, “Evaluation and comparison of current biopsy needle localization and tracking methods using 3D ultrasound,” *Ultrasonics*, vol. 73, pp. 206–220, Jan. 2017.

[30] J. L. Gennisson and G. Cloutier, “Sol-gel transition in agar-gelatin mixtures studied with transient elastography,” *IEEE Trans. Ultrason., Ferroelectr., Freq. Control*, vol. 53, no. 4, pp. 716–723, Apr. 2006.

[31] F. Zvietcovich, N. Baddour, J. P. Rolland, and K. J. Parker, “Shear wave propagation in viscoelastic media: Validation of an approximate forward model,” *Phys. Med. Biol.*, vol. 64, no. 2, Jan. 2019, Art. no. 025008.

[32] M. Gesnik *et al.*, “*In vivo* ultrafast quantitative ultrasound and shear wave elastography imaging on farm-raised duck livers during force feeding,” *Ultrasound Med. Biol.*, vol. 46, no. 7, pp. 1715–1726, Jul. 2020.

[33] M. Bhatt *et al.*, “Multiparametric *in vivo* ultrasound shear wave viscoelastography on farm-raised fatty duck livers: Human radiology imaging applied to food sciences,” *Poultry Sci.*, vol. 100, no. 6, Jun. 2021, Art. no. 101076.

[34] D. Garcia *et al.*, “Stolt’s f-k migration for plane wave ultrasound imaging,” *IEEE Trans. Ultrason., Ferroelectr., Freq. Control*, vol. 60, no. 9, pp. 1853–1867, Sep. 2013.

[35] T. Loupas, J. T. Powers, and R. W. Gill, “An axial velocity estimator for ultrasound blood flow imaging, based on a full evaluation of the Doppler equation by means of a two-dimensional autocorrelation approach,” *IEEE Trans. Ultrason., Ferroelectr., Freq. Control*, vol. 42, no. 4, pp. 672–688, Jul. 1995.

[36] T. Deffieux *et al.*, “On the effects of reflected waves in transient shear wave elastography,” *IEEE Trans. Ultrason., Ferroelectr., Freq. Control*, vol. 58, no. 10, pp. 2032–2035, Oct. 2011.

[37] J. Ophir *et al.*, “Attenuation estimation in reflection: Progress and prospects,” *Ultrason. Imag.*, vol. 6, no. 4, pp. 349–395, Oct. 1984.

[38] P. He and A. McGoron, “Parameter estimation for nonlinear frequency dependent attenuation in soft tissue,” *Ultrasound Med. Biol.*, vol. 15, no. 8, pp. 757–763, 1989.

[39] K. J. Parker, J. Ormachea, and Z. Hah, “Group versus phase velocity of shear waves in soft tissues,” *Ultrason. Imag.*, vol. 40, no. 6, pp. 343–356, 2018.

[40] X. Jacob, S. Catheline, J.-L. Gennisson, C. Barrière, D. Royer, and M. Fink, “Nonlinear shear wave interaction in soft solids,” *J. Acoust. Soc. Amer.*, vol. 122, no. 4, pp. 1917–1926, Oct. 2007.

[41] M. W. Urban and J. F. Greenleaf, “A Kramers–Kronig-based quality factor for shear wave propagation in soft tissue,” *Phys. Med. Biol.*, vol. 54, no. 19, pp. 5919–5933, Oct. 2009.

[42] S. A. Goss, L. A. Frizzell, and F. Dunn, “Ultrasonic absorption and attenuation in mammalian tissues,” *Ultrasound Med. Biol.*, vol. 5, no. 2, pp. 181–186, 1979.

[43] D. W. Park, “Ultrasound shear wave simulation of breast tumor using nonlinear tissue elasticity,” *Comput. Math. Methods Med.*, vol. 2016, May 2016, Art. no. 2541325.

[44] P. Kijanka and M. W. Urban, “Phase velocity estimation with expanded bandwidth in viscoelastic phantoms and tissues,” *IEEE Trans. Med. Imag.*, vol. 40, no. 5, pp. 1352–1362, May 2021.

[45] B. R. Chintada, R. Rau, and O. Goksel, “Nonlinear characterization of tissue viscoelasticity with acoustoelastic attenuation of shear waves,” *IEEE Trans. Ultrason., Ferroelectr., Freq. Control*, vol. 69, no. 1, pp. 38–53, Aug. 2021.

[46] P. A. Narayana and J. Ophir, “On the frequency dependence of attenuation in normal and fatty liver,” *IEEE Trans. Sonics Ultrason.*, vol. SU-30, no. 6, pp. 379–382, Nov. 1983.

[47] K. J. Parker and N. Baddour, “The Gaussian shear wave in a dispersive medium,” *Ultrasound Med. Biol.*, vol. 40, no. 4, pp. 675–684, 2014.

[48] N. Baddour, “Multidimensional wave field signal theory: Mathematical foundations,” *AIP Adv.*, vol. 1, no. 2, 2011, Art. no. 022120.

[49] M. Abramowitz and I. Stegun, *Handbook of Mathematical Functions With Formulas, Graphs, and Mathematical Tables*. Washington, DC, USA: U.S. Government Publishing Office, 1964.

[50] F. B. Palabiyik, E. Inci, R. Turkay, and D. Bas, “Evaluation of liver, kidney, and spleen elasticity in healthy newborns and infants using shear wave elastography,” *J. Ultrasound Med.*, vol. 36, no. 10, pp. 2039–2045, Oct. 2017.

[51] A. T. Trout, S. A. Xanthakos, P. S. Bennett, and J. R. Dillman, “Liver shear wave speed and other quantitative ultrasound measures of liver parenchyma: Prospective evaluation in healthy children and adults,” *Amer. J. Roentgenol.*, vol. 214, no. 3, pp. 557–565, Mar. 2020.

[52] M. D. Horeh, A. Asif, and H. Rivaz, “Analytical minimization-based regularized subpixel shear-wave tracking for ultrasound elastography,” *IEEE Trans. Ultrason., Ferroelectr., Freq. Control*, vol. 66, no. 2, pp. 285–296, Feb. 2019.

[53] D. M. Dumont and B. C. Byram, “Robust tracking of small displacements with a Bayesian estimator,” *IEEE Trans. Ultrason., Ferroelectr., Freq. Control*, vol. 63, no. 1, pp. 20–34, Jan. 2016.

[54] D. M. Dumont, K. M. Walsh, and B. C. Byram, “Improving displacement signal-to-noise ratio for low-signal radiation force elasticity imaging using Bayesian techniques,” *Ultrasound Med. Biol.*, vol. 42, no. 8, pp. 1986–1997, Aug. 2016.

Ladan Yazdani received the B.Sc. degree in electrical engineering (minor in biomedical engineering) and the M.Sc. degree in biomedical engineering from the University of Tehran, Tehran, Iran, in 2015 and 2018, respectively. She is currently pursuing the Ph.D. degree in biomedical engineering with the University of Montreal, Montreal, QC, Canada.

She joined the Laboratory of Biorheology and Medical Ultrasonics, University of Montreal Hospital Research Centre, Montreal, in 2019. Her current research interests include ultrasound imaging, ultrasound elastography, and liver diseases diagnosis by ultrasound.

Manish Bhatt received the bachelor’s degree in technology from the National Institute of Technology, Hamirpur, India, in 2011, and the Ph.D. degree in biomedical imaging from the Indian Institute of Science, Bengaluru, India, in 2017.

He was a Postdoctoral Fellow with the University of Montreal Hospital Research Centre, Montreal, QC, Canada. He is currently an Assistant Professor with IIT Guwahati, Guwahati, India. His research interests are in ultrasound imaging, photoacoustics, inverse problems, and biomedical optics.

Iman Rafati received the bachelor’s degree in computational engineering sciences and the master’s degree in biomedical engineering from the University of Tehran, Tehran, Iran, in 2014 and 2016, respectively. He is currently pursuing the Ph.D. degree in biomedical engineering with the University of Montreal, Montreal, QC, Canada, and his research with the Laboratory of Biorheology and Medical Ultrasonics, University of Montreal Hospital Research Centre, Montreal.

His current research interests are in quantitative ultrasound (QUS) imaging, elastography, and liver cancer diagnosis by QUS.

An Tang was born in Ho Chi Minh City, Vietnam, in 1977. He received the M.D. degree from the University of Sherbrooke, Sherbrooke, QC, Canada, in 2000, and the M.Sc. degree in biomedical sciences from the University of Montreal, Montreal, QC, in 2012.

He completed his radiology residency at the University of Montreal, in 2005. He pursued fellowship training in abdominal imaging at the University of Toronto, Toronto, ON, Canada, in 2006. From 2006 to 2011, he practiced as an Abdominal Radiologist at the Centre Hospitalier de l’Université de Montréal, Montreal. Supported by fellowship awards from the Fulbright Program and the Canadian Institutes of Health Research, he pursued a research fellowship in quantitative liver imaging at the University of California at San Diego, San Diego, CA, USA, from 2011 to 2012. He is currently a Clinical Scientist with the Centre de recherche du Centre hospitalier de l’Université de Montréal, Montreal, a Senior Research Scholar with the Fonds de recherche du Québec—Santé, Montreal, and a Professor of Radiology with the University of Montreal. His research interest focuses on imaging-based techniques for diagnosis and monitoring of chronic liver disease and liver cancer.

Guy Cloutier (Senior Member, IEEE) received the B.Eng. degree in electrical engineering from the Université du Québec à Trois-Rivières, Trois-Rivières, QC, Canada, in 1984, and the M.Sc. and Ph.D. degrees in biomedical engineering from the École Polytechnique of Montreal, Montreal, QC, Canada, in 1986 and 1990, respectively.

He conducted a Postdoctoral Fellow at The Pennsylvania State University, State College, PA, USA, with Prof. K. Kirk Shung. He is currently the Director of the Laboratory of Biorheology and Medical Ultrasonics, University of Montreal Hospital Research Centre, Montreal, and a Professor with the Department of Radiology, Radiation Oncology, and Nuclear Medicine, and the Institute of Biomedical Engineering, University of Montreal, Montreal. He has authored more than 230 peer-reviewed articles, holds several patents, and licensed four technologies. His research interests are in quantitative ultrasound imaging, quasi-static and dynamic ultrasound elastography, development of multiphysics imaging methods, and biomechanical modeling.

Dr. Cloutier was a recipient of the National Scientist Award of the Fonds de la Recherche en Santé du Québec. He was the Associate Editor-in-Chief from 2019 to 2022, has been an Associate Editor of IEEE TRANSACTIONS ON ULTRASONICS, FERROELECTRICS, AND FREQUENCY CONTROL since 2013, and was an Academic Editor of *PLOS One*, an Invited Associate Editor of *Medical Physics*, and a member of the International Advisory Editorial Board of Ultrasound in Medicine and Biology for 15 years.